Journal of Thermal Science Vol.28, No.2 (2019) 306−318

https://doi.org/10.1007/s11630-018-1057-5 **Article ID: 1003-2169(2019)02-0306-13**

Energy Loss Analysis of Novel Self-Priming Pump Based on the Entropy Production Theory

CHANG Hao[1], SHI Weidong[1,2*], LI Wei[1*], LIU Jianrui[1]

1. Research Center of Fluid Machinery Engineering and Technology, Jiangsu University, Zhenjiang, 212013, China
2. School of mechanical engineering, Nantong University, Nantong 226019, China

© Science Press, Institute of Engineering Thermophysics, CAS and Springer-Verlag GmbH Germany, part of Springer Nature 2018

Abstract: The conventional method cannot explicitly confirm the location and type of the energy loss, therefore this paper employs the entropy production theory to systematically analyze the category, magnitude and location of hydraulic loss under different blade thickness distribution. Based on the analysis, the turbulent entropy and viscosity entropy produced by the separation of boundary layer at the trialing edge are major factors leading to the hydraulic loss. In addition, the separation of the boundary layer can not only cause the energy loss, but also block the passage of the impeller and reduce the expelling coefficient of the blade. Therefore, the hydraulic performance of the blades with increment thickness distribution is obviously better than the decrement one. Further, the flow rate has different influence on the three types of entropy production. Meanwhile, the pressure pulsation on the working surface was investigated. It was concluded that with flow rates increasing, the amplitude of pressure pulsation firstly decreases and then smoothly improves, and reaches the minimum under design flow rate. Finally, the optimal blade was obtained, and the relevant hydraulic performance test was performed to benchmark the simulation result. This research can provide the theoretical reference for designing the reasonable thickness distribution of the blades.

Keywords: entropy production, energy loss, thickness distribution, pressure pulsation

1. Introduction

With the variation of the global climate, the water resource shortage is becoming the noticeable restriction of the agricultural production. Therefore, it is imperative to improve the irrigation efficiency to ensure the water demands of crops [1-2]. However, the irrigation efficiency is limited by the pump energy loss. In recent years, numerous efforts have been made in reducing the energy loss of the pump by test and numerical simulation. Wang et al. [3] combined the computational fluid dynamics and energy loss model to analyze the energy loss mechanism of multistage centrifugal pump. Sung et al. [4] investigated the efficiency loss of the double-suction centrifugal pump with different internal surface roughness, and found that roughness of the outward shroud surface exerts a great effect on the pump performance. Zhang et al. [5] proposed a novel design method of the impeller based on the quasi-3D hydraulic design, the boundary vortex flux diagnosis and the genetic algorithm, while the relevant hydraulic performance tests were conducted, the efficiency of the optimized

Received: May 23, 2018
Corresponding author: SHI Weidong E-mail: Wdshi2012@126.com
LI Wei lwjiangda@ujs.edu.cn

impeller are increased by 2.5%. Wang et al. [6] designed the forward-curved blades, and studied the influence of the blade inlet angles on the energy loss within the impeller. Jeon et al. [7] selected the impeller upper blade height and hub height as the design variables to study the efficiency and pressure under the operating flow condition. Li et al. [8] assessed the hydraulic and cavitation performance of engine cooling water pump based on the blade outlet widths (11 mm, 13 mm and 16 mm).

However, most previous researches concentrated on the improvement of efficiency through adjusting the geometrical parameters of the impeller; few researchers analyze the thickness distribution of the blades to reduce the energy loss. Meanwhile, due to the limitations of the traditional methods, it is difficult to indicate the type and the location of the energy loss. Therefore, the entropy production theory is introduced to analyze the hydraulic loss of pump. In 1983, Bejan et al. [9] investigated the entropy generation minimization based on considerable researches. Li et al. [10] studied the hysteresis characteristic of the pump and proposed the wall equation based on the wall effects of entropy production. Hou et al. [11] presented the hydraulic loss of Liquefied Natural Gas (LNG) cryogenic submerged pump, and obtained the magnitude and location of the different entropy generation rate. Herwig et al. [12-13] analyzed the influence of different roughness wall on the entropy production, and distinguished the four entropy production sources. Pei et al. [14] simulated the six low-head pumps with different distances between impeller and guide vane, and hydraulic loss mechanisms were obtained by employing the entropy production method. Hence, the entropy production theory is an effective method to investigate the energy loss of the internal flow.

This paper proposes a novel self-priming pump to improve the efficiency of self-priming. Meanwhile, in order to investigate the energy loss of the internal flow field, entropy production theory is introduced. The three types of energy loss under different thickness distribution blades are obtained, and the pressure pulsation on the working surface of the blades are analyzed. The performance test of optimal design was conducted to benchmark the numerical simulation. Finally, the reasonable thickness distribution of the blade is recommended.

2. Structure and Mechanism of Novel Self-Priming Pump

As shown in Fig. 1, the novel self-priming pump is comprised by jet self-priming system, the compressor and pump. The jet self-priming system consists of nozzle A, the nozzle C, inlet round turnbuckle B, globe valve, filter, vent hose and hose connectors (Fig. 2).

The high-speed air is generated in the compressor and injected into the jet self-priming system through hose. The cross section of the nozzle C firstly decreases sharply and then increases smoothly. Hence, the velocity of the air is obviously enhanced after flowing through the nozzle C, and the negative pressure is created near the inlet round turnbuckle B, which leads to that the air in the value box is carried out with the high-speed air into the nozzle A and discharges to the atmosphere. Consequently, the negative pressure is generated in the value box. When the pressure upon the globe valve is larger than the gravity, the globe value is separated from the value seat, and the air in the value box is connected with the pump by the through-hole of value seat. Finally, with the declines of the air, the pump is filled with water. When the globe valve is submerged in the water, it will fall back to the value seat and block the through-hole, and then the self-priming process is accomplished. In this system, the well cooperation between jet nozzle and the globe value can achieve quickly self-priming velocity and the self-closing.

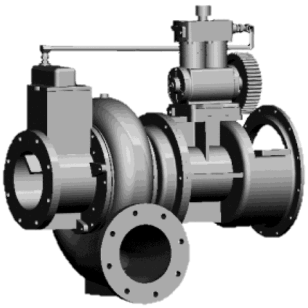

Fig. 1 Structure of the novel self-priming pump

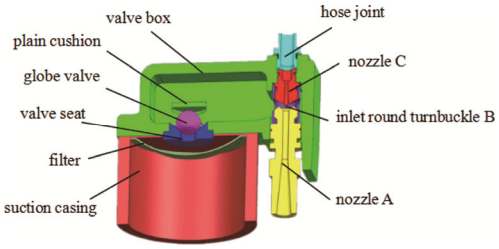

Fig. 2 Structure of the jet self-priming system

The blade, as a necessary working unit of the novel self-priming pump, plays an essential role in the energy conversion. In this paper, the blades are designed based on the empirical correlation equation, which is obtained by plenty of outstanding hydraulic models. The design specifications of the novel jet self-priming pump are shown as follow: Q = 500 m^3/h, head H = 45 m, rotation speed n = 2200 r/min and specific speed n_s = 172. Table 1

lists the principal geometric parameters of the pump. Nine different thickness distribution blades are proposed relied on the casting technique and engineering experience [15], and the schemes with different blade thickness distribution are shown in Table 2.

Table 1 Principal geometric parameters of the pump

Impeller outlet diameter	Impeller inlet diameter	Impeller outlet width	Number of blade
280 mm	200 mm	44 mm	6

Table 2 Blades with different thickness distribution

Scheme	Thickness of leading edge/mm	Thickness of middle part /mm	Thickness of trailing edge /mm
1	3	3	3
2	6	6	6
3	3	6	3
4	3	4.5	6
5	6	4.5	3
6	3	6	6
7	6	6	3
8	3	3	6
9	6	3	3

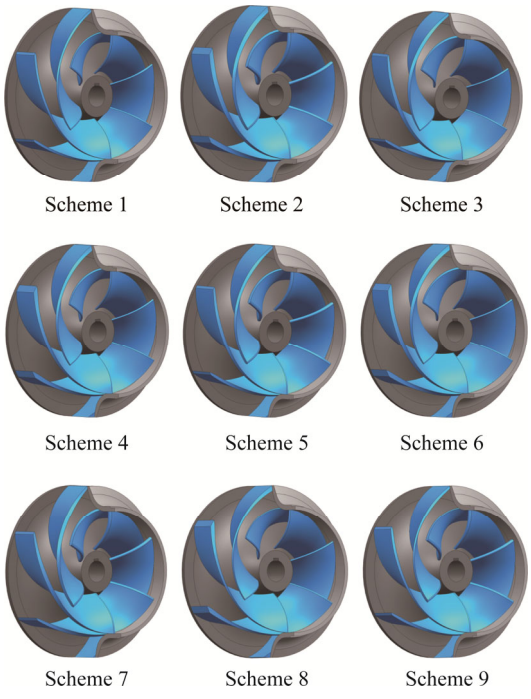

Fig. 3 The 3D model of blades with different thickness distribution

3. Analysis Model and Numerical Method

3.1 Computational domain and method

As shown in Fig. 4, the computational domains of the self-priming pump are composed with inlet, impeller, volute, outlet and suction casing of self-priming system. In order to obtain the stable incoming flow and fully developed outflow, the inlet and outlet were extended five times of the pipe diameter respectively. ANSYS CFX was employed to perform the numerical calculation; the SST k-ω is chosen as the turbulence model [16], and normal temperature water as the flow media. The computational domains of the inlet, volute, outlet and suction casing of self-priming system were set as the stationary one, while the domain of impeller was set as rotation. The interfaces between impeller with inlet and suction casing of self-priming were set as the frozen rotor interfaces, while other interfaces were set as general grid. In order to reflect practical surface of the pump, the wall roughness was selected as 50 μm, and the boundary of the inlet and outlet were set as total pressure and mass flow, respectively. In addition, the high resolution was adopted as advection scheme, and the convergence of the residuals was set as 0.00001.

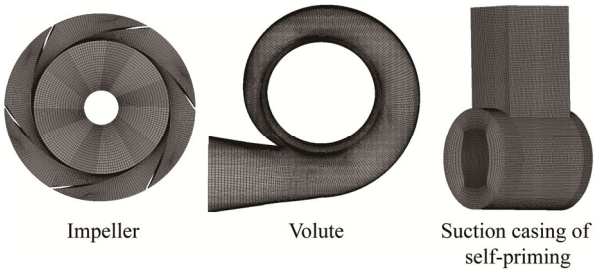

Fig. 4 Computational domains

3.2 Grid generation

The quantity and quality of the grid play an important role in credibility of simulation [16]. With the grid quantity increasing, the deviation of simulation gradually declines, but considerable time and the expensive simulation resources are consumed. Therefore, it is imperative to select a reasonable grid number. In this paper, the structured grids are employed to discretize the calculation domain. The grid independency analysis was conducted.When the number of the elements exceeded 2671710, fluctuation of the head and efficiency is less than 1%, and Y+ ≤ 60. The suitable element numbers of inlet, outlet, volute, impeller and suction casing of self-priming system are 504000, 696000, 720480, 478998 and 272232, respectively.

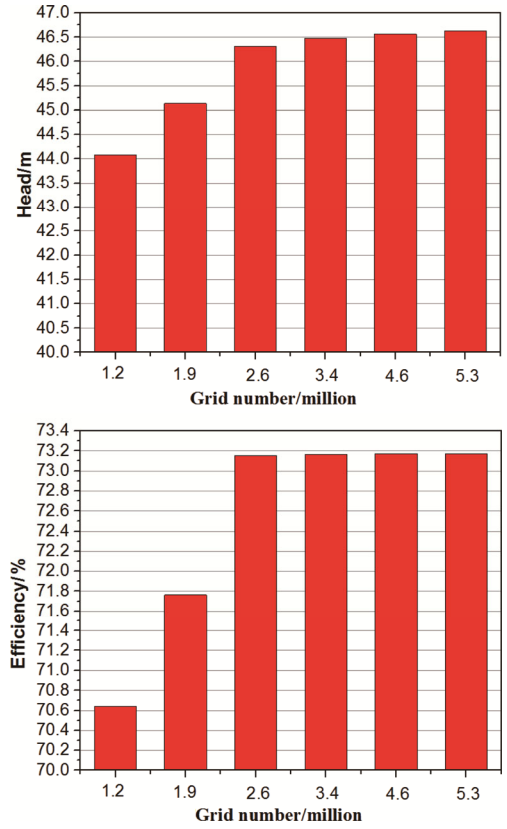

Fig. 5 Analysis of grid independent

4. Analysis of Simulation Results

4.1 Analysis of the pressure distribution

The pressure distribution on the working surface within four conditions is shown in Fig. 6. Owing to that the blades transform the kinetic energy into the potential energy, the pressure on working surface increases from leading edge to trailing edge, and the local low-pressure is generated in the leading edge of blade where is prone to cause the cavitation. In Fig. 6 (a), it is interesting to find that an obvious elliptical high-pressure area (EHPA) exists at the trialing edge of the blade under Q = 100 m^3/h. The thickness distribution of the blade is different, which leads to a diversity of the magnitude of EHPA. At the same time, the EHPA of the blades with decrement thickness distribution (scheme 2, 3, 5, 7 and 9) is larger than the blades with increment thickness distribution (scheme 1, 4, 6 and 8), and the scheme 2 reaches the maximum at Q = 100 m^3/h.

With the flow rate increasing to 300 m^3/h, the intensity of the EHPA at the trialing edge of the blade is improved, while the area of EHPA and the low-pressure at the leading edge of the blades significantly decreases. The reason for above results are ascribed to that the flow in the impeller are comprised by the uniform flow and axial vortex flow. When the pump operates under small flow rates, the two flows are in the opposite direction on the working surface of the blade, which results in the relative low velocity near the working surface. Therefore, the positive angle of attack is generated, leading to the

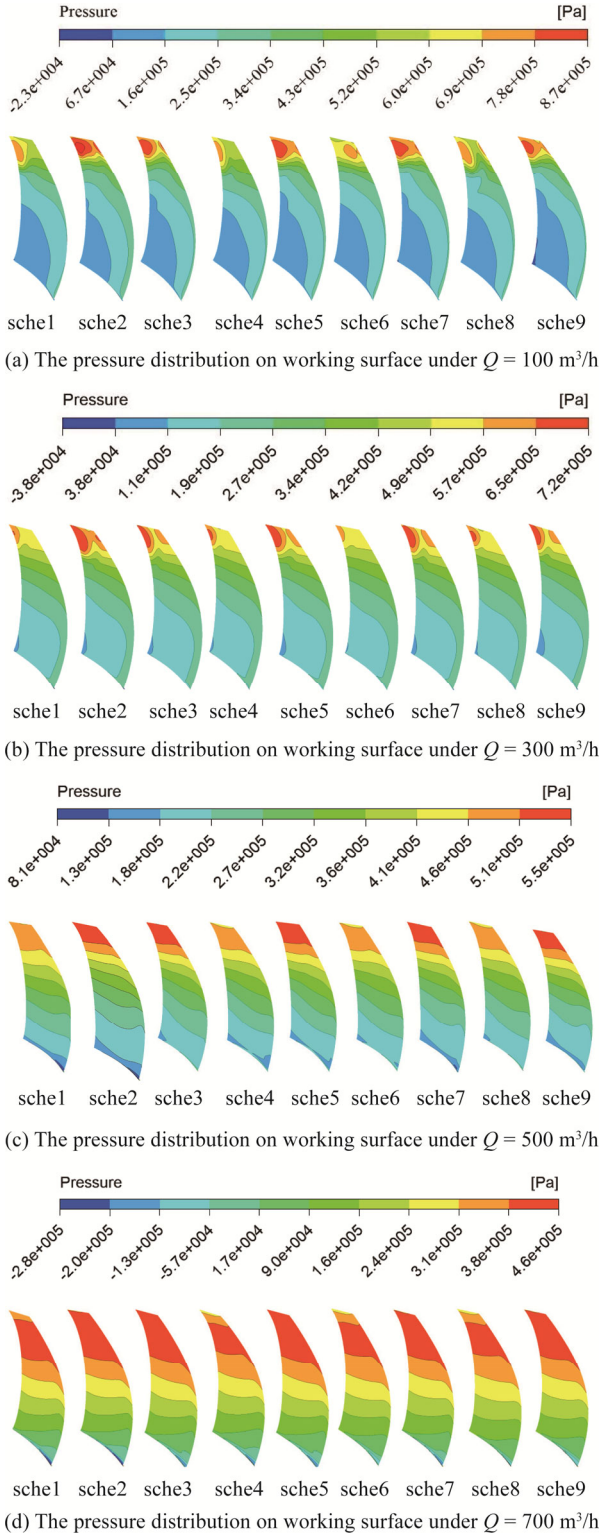

(a) The pressure distribution on working surface under Q = 100 m^3/h

(b) The pressure distribution on working surface under Q = 300 m^3/h

(c) The pressure distribution on working surface under Q = 500 m^3/h

(d) The pressure distribution on working surface under Q = 700 m^3/h

Fig. 6 The pressure distribution on working surface

insufficient control of the fluid boundary layer on the working surface, thus the separation of unstable boundary layer at the blade trialing edge is occurred. Due to the difference in blades thickness, inducing the discrepancy of the attack angle on the working surface of blade, so the intensity of EHPA also exists difference.

Fig. 6 (c) presents the different negative pressure at the leading edge of working surface under Q = 500 m^3/h. As the thickness of the blade leading edge in scheme 2, 5, 7 and 9 is thicker, the meridional velocity is improved and the blade expelling coefficient is reduced. Meanwhile, the negative pressure of the scheme 2, 5, 7 and 9 is more obvious. What is more, the EHPA of each scheme on the working surface vanishes at the design flow rate. When the flow rate increases to the 700 m^3/h, gradient of pressure distribution on the working surface becomes more uniform. But with increment thickness distribution of the trailing edge of working surface, the local low-pressure occurred. The relative velocity at the trialing edge is high under large flow rates, and the movement of liquid in volute based on free vortex theory, the velocity vector at the blade trailing edge changes significantly. Hence, the local low-pressure can be found at the trailing edge of the blade with increment thickness distribution.

Importantly, more attention should be paid to EHPA on the trailing edge of the working surface; it not only leads to the irreversible transformation of energy into thermal effect, which causes the hydraulic loss, but also blocks the passage of blade, decreasing the expelling coefficient and the ability of streaming. Therefore, entropy production theory is introduced to analyze the hydraulic loss in the pump, which can give a reference for designing the thickness of the blades based on the hydraulic loss minimization.

4.2 Entropy production theory

Entropy production analysis is a method based on the second law of thermodynamics, which combines the heat transfer theory and hydrodynamics to calculate the actual process of energy loss. Entropy production represents the irreversibility of the system and the magnitude of energy loss in flow. The entropy production is comprised by four parts: viscosity entropy production, turbulent entropy production, wall entropy production and temperature entropy production. Considered that the entropy production is the state parameter, the entropy production rate is introduced to express the transport equation of incompressible fluid [17].

$$\rho\left(\frac{\partial s}{\partial t}+u\frac{\partial s}{\partial x}+v\frac{\partial s}{\partial y}+w\frac{\partial s}{\partial z}\right)=div\left(\frac{\vec{q}}{T}\right)+\frac{\Phi}{T}+\frac{\Phi_\Theta}{T^2} \quad (1)$$

where s is the entropy production; u, v and w are the velocity on three directions (x, y and z) respectively; $\vec{q}$ is the density of heat flow rate; Φ represents the entropy production generated by the viscous dissipation, Φ_θ stands for the entropy production generated by the temperature variation. The temperature entropy production can be ignored in the operation as the temperature variation in the self-priming pump is slight. Gong et al. [18] proposed the formulae which can directly calculate the viscous dissipation of the incompressible fluid:

$$\Phi=\mu\left[2\left(\frac{\partial u}{\partial x}\right)^2+\left(\frac{\partial v}{\partial y}\right)^2+\left(\frac{\partial w}{\partial z}\right)\right]+\left[\left(\frac{\partial u}{\partial y}+\frac{\partial v}{\partial x}\right)^2+\left(\frac{\partial u}{\partial z}+\frac{\partial w}{\partial x}\right)^2+\left(\frac{\partial v}{\partial z}+\frac{\partial w}{\partial y}\right)^2\right] \quad (2)$$

Since the transient motion is the superposition of the time average motion and fluctuating motion, the entropy production rate can be divided into the time average entropy production and fluctuating entropy production [13]:

$$s_{VD}=\frac{\mu}{T}\left[2\left\{\left(\frac{\partial \overline{u}}{\partial x}\right)^2+\left(\frac{\partial \overline{v}}{\partial y}\right)^2+\left(\frac{\partial \overline{w}}{\partial z}\right)^2\right\}+\left(\frac{\partial \overline{u}}{\partial y}+\frac{\partial \overline{v}}{\partial x}\right)^2+\left(\frac{\partial \overline{u}}{\partial z}+\frac{\partial \overline{w}}{\partial x}\right)^2+\left(\frac{\partial \overline{v}}{\partial z}+\frac{\partial \overline{w}}{\partial y}\right)^2\right] \quad (3)$$

$$s_{TD}=\frac{\mu}{T}\left[2\left\{\overline{\left(\frac{\partial u'}{\partial x}\right)^2}+\overline{\left(\frac{\partial v'}{\partial y}\right)^2}+\overline{\left(\frac{\partial w'}{\partial z}\right)^2}\right\}+\overline{\left(\frac{\partial u'}{\partial y}+\frac{\partial v'}{\partial x}\right)^2}+\overline{\left(\frac{\partial u'}{\partial z}+\frac{\partial w'}{\partial x}\right)^2}+\overline{\left(\frac{\partial v'}{\partial z}+\frac{\partial w'}{\partial y}\right)^2}\right] \quad (4)$$

where s_{VD} stands for entropy production rate generated by viscosity dissipation; s_{TD} stands for entropy production rate generated by turbulent dissipation.

As the fluctuating velocity is difficult to measure, Herwig et al. [12] established a model by employing the rate of turbulent dissipation instead of the fluctuating velocity field. The model established the relationship between the turbulent dissipation rate and entropy production:

$$s_{TD}=\frac{\rho\varepsilon}{T} \quad (5)$$

where ρ represents the density of fluid; ε stands for the turbulent dissipation rate.

Due to the effect of viscosity, there exists obvious velocity gradient on the wall surface, when the fluid transition from the turbulence core region to the laminar boundary layer. Calculation error is generated by employing the formula of the viscosity entropy. Therefore, it is necessary to calculate the entropy production at the wall separately. Zhang et al. [19] gave a method to calculate the entropy generation of wall. The fluid

velocity on the wall is assumed to zero, and the entropy generated by the fluid near the wall can be solved by integrating the entropy production rate of the wall region:

$$S_W = \int_S \frac{\tau_W v_p}{T} dS \tag{6}$$

where S_W stands for wall entropy production rate, τ_W is wall shear stress; v_P is the average velocity of fluid at the center of the first layer near the wall.

$$S_{TD} = \int_V s_{td} dV \tag{7}$$

$$S_{VD} = \int_V s_{vd} dV \tag{8}$$

The total viscosity entropy production and turbulent entropy production can be calculated through formulae (7) and (8), that is, to sum the entropy production of each grid volume in the computational domain.

Fig. 7 shows the relationship between flow rates and viscosity entropy production based on the entropy production theory, which indicates that the viscosity entropy production raises smoothly with the flow rate growing, except for the scheme 2 and 5 with rapid increase. The rising rate of scheme 2 is obviously larger than other schemes, which still improves with the increase of the flow rates. Meanwhile, the turbulent entropy production of each schemes within different flow rates are shown in Fig. 8, and the amount of turbulent entropy production declines with the rising of flow rate. The linear relationship between the turbulent entropy production and flow rates is generated from 0.2Q to 1.0Q, while the rate of reduction is decreasing from 1.0Q to 1.4Q, and the minimum rate of variation is obtained at the 1.4Q. What is more, the turbulent entropy production of scheme 2 under 0.2Q is obviously larger than other schemes.

Fig. 9 indicates the wall entropy production for different flow rate conditions. The wall entropy production first declines and then rises, and the minimum is obtained at about 0.9 Q condition. In general, the decrease rate is less than increase rate. The minimum of wall entropy production with thick thickness blades (scheme 2) is significantly larger than thin thickness blades (scheme 1). By comparing the three types of entropy production within different flow rates, it is concluded that the flow rate can influence the entropy production. The turbulent entropy production and viscosity entropy production are greater than the wall entropy production, which can be regarded as the major factors leading to energy loss. Considering the working surface of the blades plays an important role in the energy transmission from mechanical energy to the internal energy of water, therefore, the distributions of turbulent entropy production rate and viscosity entropy production rate on the working surface are analyzed.

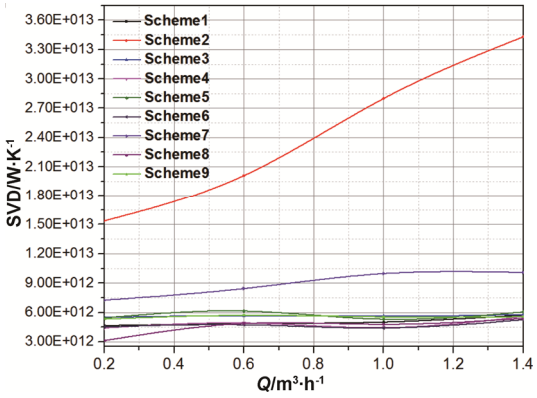

Fig. 7 The viscosity entropy production

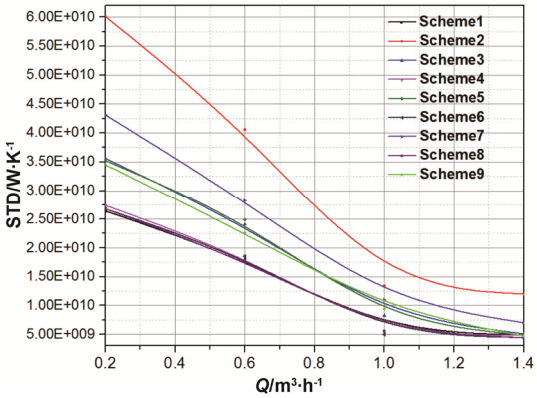

Fig. 8 The turbulent entropy production

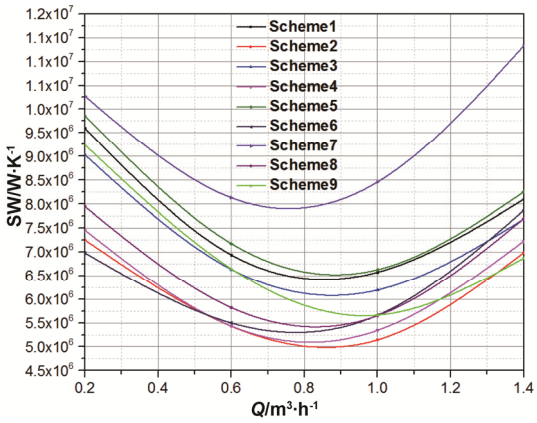

Fig. 9 The wall entropy production

4.3 Distribution of the viscosity entropy production rate on working surface

Distribution of viscosity entropy production rate within four flow rates is shown in the Fig. 10. The viscosity entropy production is mainly caused by the irreversible viscous dissipation, and the large area of viscous dissipation is found at the trailing edge of the

working surface under the small flow rates (0.2Q and 0.4Q). Meanwhile, due to the relatively low velocity of water flow through the blade under small flow rates with a positive attack angle on the working surface, the boundary layer is separated; the stability of the internal flow is destroyed and the viscous dissipation is caused. Therefore, the viscous dissipation of the thick blade scheme 2, 5 and 7 is obviously higher than that of other cases. With the increase of flow rates, the positive angle of attack gradually declines and the area of the boundary layer separation decreases. Moreover, the leading edge of the scheme 2, 5 and 7 are thicker than other schemes, and the overcurrent area of impeller is reduced, which results in that the working surface exists obvious flow impact within the large flow rates, and the high viscous dissipation are generated at the leading edge of the scheme 2, 5 and 7. Contrarily, viscous dissipation of the scheme 6 is the lowest, because the increment of blade thickness from leading edge to the trailing edge will not only decrease the positive attack angle under the small flow rates, but also decline the flow impact on the inlet of the impeller.

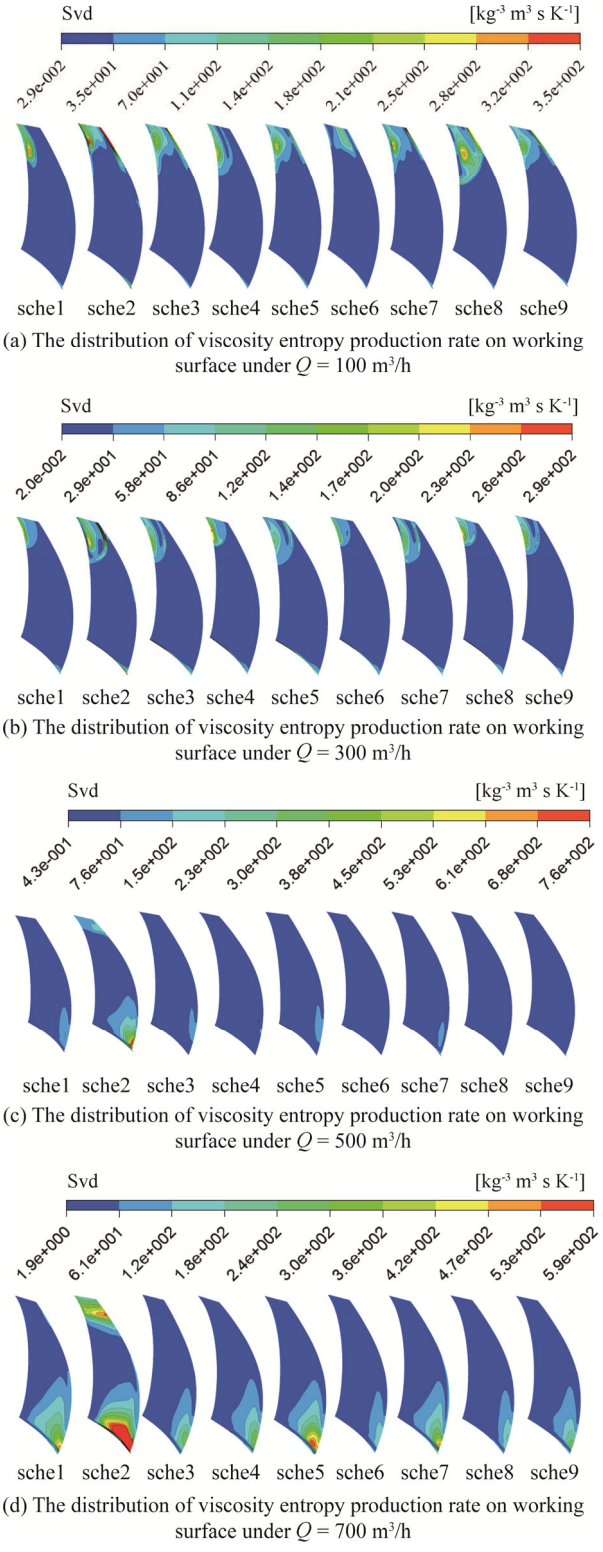

Fig. 10 The distribution of viscosity entropy production rate

4.4 Distribution of the turbulent entropy production rate on working surface

The distribution of turbulent entropy production rate on the working surface is presented in Fig. 11. Compared with the viscosity entropy production rate, the turbulent entropy production rate is quite small. The turbulent dissipation is related to the turbulent entropy production. A large turbulent entropy production region can be observed at the trailing edge of the working surface under small flow rates. What is more, the turbulent dissipation on the working surface of the scheme 2 is much more serious than other schemes, which ascribes to that the separation of boundary layer blocks the impeller passage, thus the turbulent vortexes are generated at the trailing edge of the working surface. At the same time, with the increase of the flow rates, the smaller attack angles are formed on the working surface, which leads to the decrease of the boundary layer separation and turbulent vortexes.

Therefore, according to the theory of the entropy production, it is concluded that the thickness distribution of the blade plays a decisive role in the energy loss. Compared with the energy loss of the different thickness distribution blade, the blade with the decrement distribution thickness can not only lead to obvious separation of the boundary layer small flow rates, but also generates the strong impact on the leading edge under large flow conditions. On the contrary, the turbulent entropy production and viscosity entropy production of the blade with increment thickness distribution are lower than the decrement one. More importantly, the energy loss of the scheme 6 with increment thickness distribution is the lowest among the nine schemes. In other words, the blade thickness distribution of 3-6-6 is more in line with the regularity of ideal liquid flow.

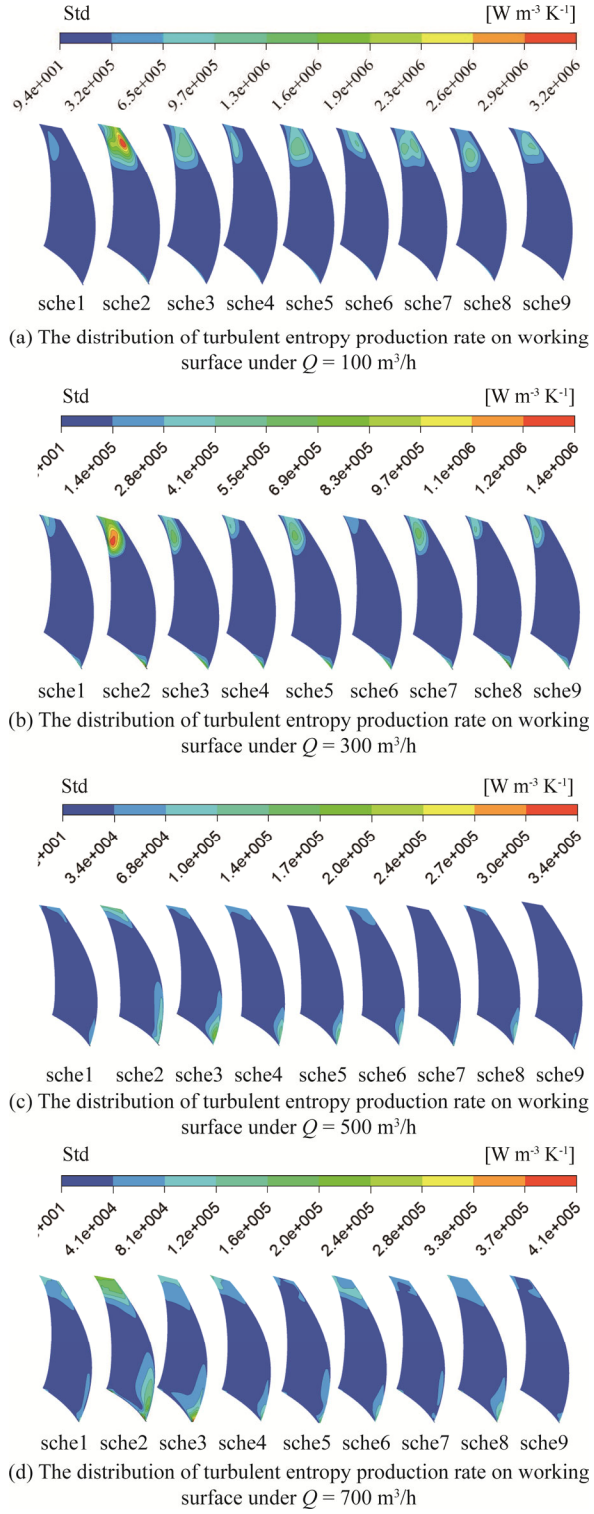

(a) The distribution of turbulent entropy production rate on working surface under Q = 100 m³/h

(b) The distribution of turbulent entropy production rate on working surface under Q = 300 m³/h

(c) The distribution of turbulent entropy production rate on working surface under Q = 500 m³/h

(d) The distribution of turbulent entropy production rate on working surface under Q = 700 m³/h

Fig. 11 The distribution of turbulent entropy production rate

5. The Analysis of Hydraulic Performance

The head, as an important index of the fluid machine, reflects the energy gained from pump by unit mass liquid. The equation of the head can be represented as:

$$H = \frac{p_d - p_s}{\rho g} + \frac{v_d^2 - v_s^2}{2g} + (z_d - z_s) \tag{9}$$

where P_d and P_s stand for the liquid pressure of the pump outlet and inlet respectively; v_d and v_s represent the liquid velocity of the pump outlet and inlet respectively; Z_d and Z_s represent the distance from the inlet and outlet of pump to the base level respectively.

In order to reduce the deviation, the non-dimensional treatment is carried on the head and flow rates. The non-dimensional head and flow rates can be given as:

$$\phi = \frac{Q}{\pi D_2 b_2 u_2} \tag{10}$$

$$\psi = \frac{gH}{u_2^2/2} \tag{11}$$

where Q is the flow rates; n is the rotation speed; D_2 is the impeller outer diameter; H is the head of the pump; b_2 is the impeller outlet width; u_2 is the circumferential velocity at the impeller outlet which can be obtained as follow:

$$u_2 = \frac{\pi D_2 n}{60} \tag{12}$$

Eq. (12) is substituted into Eq. (10) and Eq. (11):

$$\phi = \frac{60Q}{\pi^2 D_2^2 b_2 n} \tag{13}$$

$$\psi = \frac{2gH \times 3600}{\pi^2 D_2^2 n^2} \tag{14}$$

As illustrated in Fig. 12, the head of the blades with increment thickness distribution is obviously larger than that of the blades with decrement thickness distribution. This phenomenon is ascribed to the increase of meridional velocity and angle of attack with the decrease of the thickness distribution of blades, and the boundary layer is severely separated, leading to significant viscosity entropy production. At the same time, the separation of the boundary layer can not only cause the energy loss, but also block the passage of the impeller and reduce the expelling coefficient of the blade. Therefore, the head of the scheme 1 is lower than scheme 2 from 250 m³/h to 450 m³/h, which is caused by the collision of the liquid, rather than energy conversion through blades. As shown in the Fig. 13, although the head of the uniform thick blade of scheme 2 is higher than that of the thin blade of scheme 1, the efficiency of the liquid collision is still lower than the thinner blade, considering that the impact of the liquid is accompanied by severe viscosity dissipation. Importantly, the hydraulic performance of the blades with increment blades thickness distribution is better than that of scheme 1 with thin blades, which indicated that the preferable hydraulic characteristics can be obtained by applying the blades with increment blades thickness distribution. Therefore, the thickness

distribution of blades is of great significance to internal flow field of the impeller.

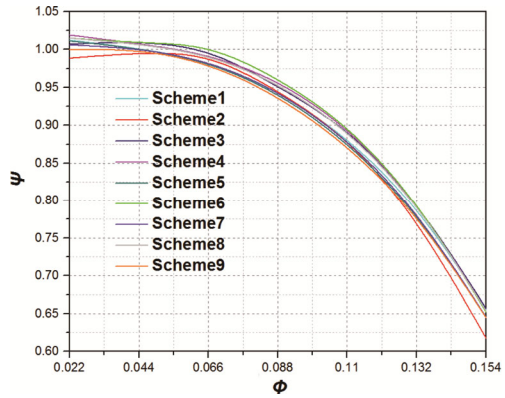

Fig. 12 Head curves of each scheme

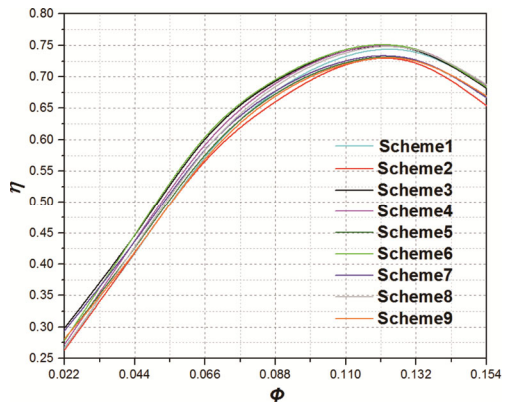

Fig. 13 The efficiency curves of each scheme

6. Analysis of the Pressure Pulsation

The axial or radial vibration of the blades can be generated under the effect of unsteady flow conditions, and the vibration can not only lead to the fatigue failure, but also cause the crack on the working surface, which can affect the service life of the impeller seriously. In order to ensure the high-efficiency and safety operation of the blades for a long time, the pressure fluctuation of the impeller is analyzed, which can present the unsteady characteristic of the flow field on the working surface clearly. Due to that the wrapping angle of the blade is 120°, the monitoring points are set on the middle streamline of the working surface every 20° from leading edge to the trailing edge (P_0, P_1, P_2, P_3, P_4 and P_5), as shown in Fig. 14.

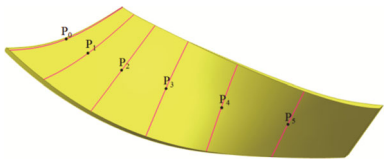

Fig. 14 Location diagram of pressure monitor points

The unsteady calculation is carried out on the basis of the steady simulation result, the blade rotation speed is set as 2200 r/min, and the total simulation time is 0.22 s. Meanwhile, a time step is obtained when the blades rotate 3°, namely, every time step will cost 2.27×10^{-4} s. In order to acquire the convergent results, the pressure fluctuation data of the 9th rotation period are analyzed. At the same time, the pressure coefficient C_p is introduced to reduce the deviation caused by the nonuniform variation of the pressure. The transient pressure of the grid node comprises two parts, namely, the time-averaged pressure and periodic pressure [20-22]:

$$\overline{p}(node)=\frac{1}{N}\sum_{j=0}^{N-1}p(node,t_0+j\Delta t) \tag{15}$$

$$\tilde{p}(node,t)=p(node,t)-\overline{p}(node) \tag{16}$$

$$C_P=\frac{\sqrt{\frac{1}{N}\sum_{j=0}^{N-1}\tilde{p}^2(node,t+\Delta t)}}{\frac{1}{2}\rho U_2^2} \tag{17}$$

Where $\overline{p}$ is the time-averaged pressure; $\tilde{p}$ is periodic pressure; N is total time step; Δt is the time step; ρ is the density of water; U_2 is the rotation velocity at the outlet of impeller.

The time domain diagrams of pressure pulsation are shown in Fig. 15. It can be found that the pressure pulsation of each scheme has the similar variation rule within the same flow rate. The pressure pulsation amplitude is increasing from leading edge to the trailing edge, and the pressure pulsation amplitude of P_5 reaches the maximum among the six monitoring points. The pressure pulsation phase of P_5 is significantly lagged behind the other pressure monitoring points. It can be seen that the flow rate plays an important role on the characteristics of pressure pulsation, and the pressure pulsation amplitude under the small flow rates is obviously higher than other flow rates. Meanwhile, the boundary layer separation blocks the impeller passage, causing the pressure wave to collide with the flow, resulting in secondary peak at small flow rate. What is more, the amplitude of the secondary wave can be enhanced when the fluctuation mode is identical to the separation of boundary layer; otherwise, the amplitude of the secondary wave is very low. With the increase of the flow rates, the separation of boundary layer gradually disappears, and the amplitude of pressure pulsation reaches the minimum under the design flow rate. At the same time, the waveform would be transformed from the irregular wave to the sine wave. However, when the flow rates increase continuously, the amplitude of pressure pulsation rises slightly without any secondary wave. The same conclusions are obtained by Zhai et al. [22]

Fig. 15 indicates that the pressure pulsation amplitude of the blade with increment thickness distribution is larger than the increment one under design and large flow

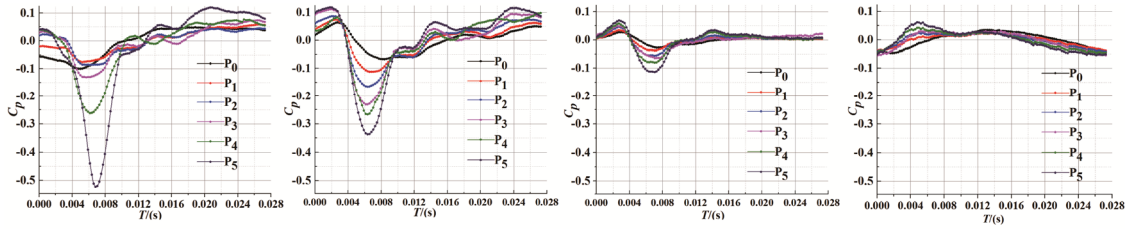

Q = 100 m³/h Q = 300 m³/h Q = 500 m³/h Q = 700 m³/h

(a)The pressure coefficient C_p of scheme 1

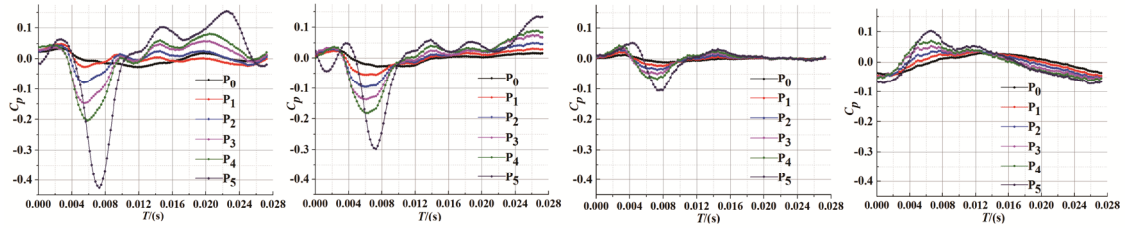

Q = 100 m³/h Q = 300 m³/h Q = 500 m³/h Q = 700 m³/h

(b)The pressure coefficient C_p of scheme 2

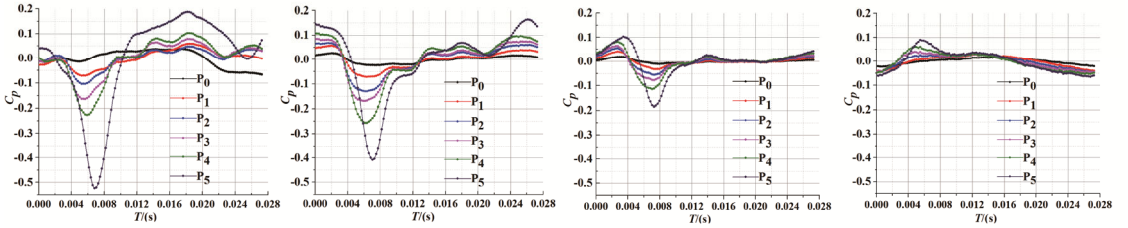

Q = 100 m³/h Q = 300 m³/h Q = 500 m³/h Q = 700 m³/h

(c)The pressure coefficient C_p of scheme 3

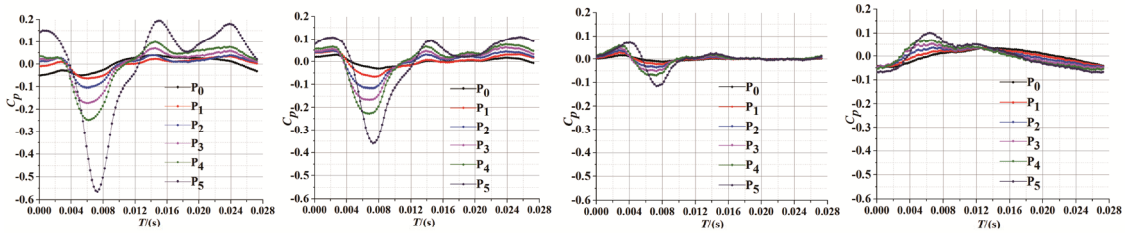

Q = 100 m³/h Q = 300 m³/h Q = 500 m³/h Q = 700 m³/h

(d) The pressure coefficient C_p of scheme 4

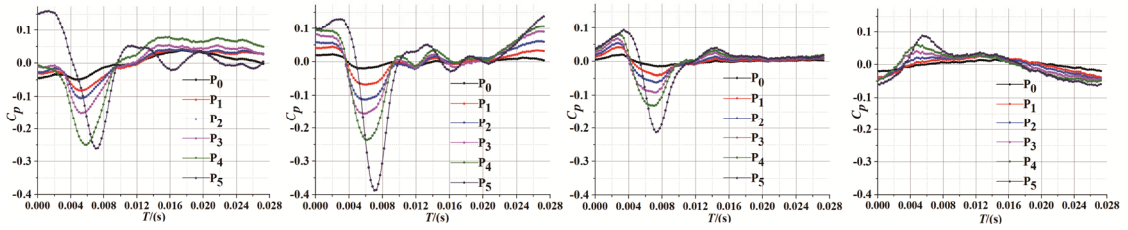

Q = 100 m³/h Q = 300 m³/h Q = 500 m³/h Q = 700 m³/h

(e) The pressure coefficient C_p of scheme 5

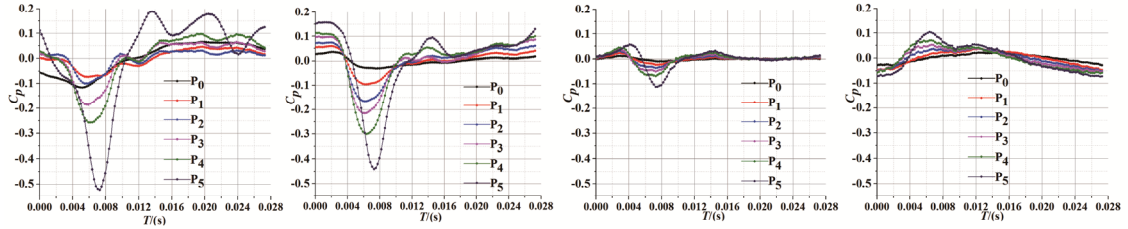

Q = 100 m³/h Q = 300 m³/h Q = 500 m³/h Q = 700 m³/h

(f) The pressure coefficient C_p of scheme 6

Continuation Fig. 15

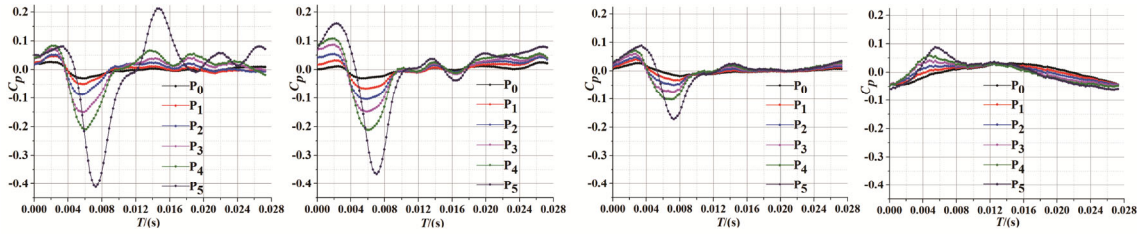

(g) The pressure coefficient C_p of scheme 7

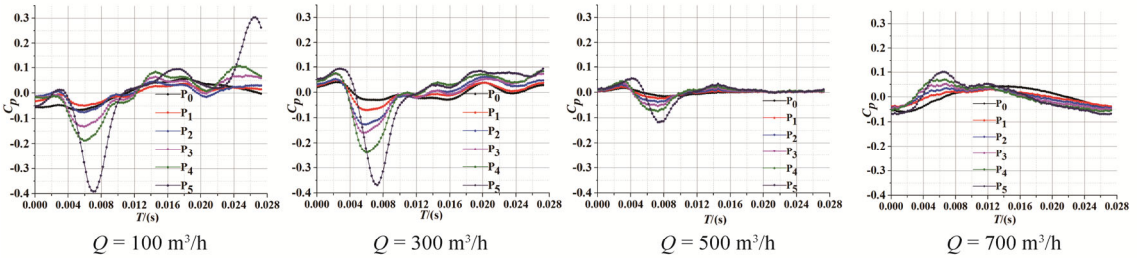

(h) The pressure coefficient C_p of scheme 8

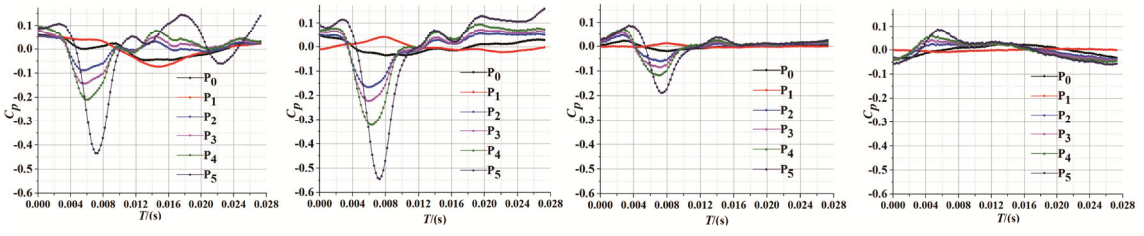

(i) The pressure coefficient C_p of scheme 9

Fig. 15 Time domain diagrams of pressure pulsation

rate, but the condition is opposite under the small flow rates. Furthermore, the amplitude of pressure fluctuation of scheme 6 is obviously lower than other schemes under design flow rate. In other word, the blade with thickness distribution of 3-6-6 can satisfy the requirements of the ideal liquid flow, and the liquid could flow according to the designed speed direction. Therefore, the thickness distribution of the blades can effectively improve the pressure pulsation characteristics, and ensure the blades operating under the safe and stable condition.

7. Test

7.1 Test of hydraulic performance

In order to benchmark the result of simulation, the test of optimal blade with increment thickness distribution (3-6-6) are carried out on the I level accuracy test bench in Jiangsu University, as shown in Fig. 16. All experiment instruments are employed after calibration. Table 3 lists the accuracy of apparatus.

Fig. 17 presents the external characteristic curves of the novel self-priming pump based on the simulation and test. The performance curve obtained by numerical computation is more in line with test results within different flow rates. The deviations are less than 3%, which is attributed to the neglect of mechanical loss of seals and bearings in the numerical computation. Thus, the internal field characteristics of the novel self-priming pump can be predicted reasonably through appropriate grid quality and turbulence model.

Table 3 Accuracy of apparatus

Apparatus	Accuracy
Turbine flow meter	±1.0%
Pressure sensor	±0.5%
Torque-speed transducer	±0.5%

Fig. 16 The test of external characteristic

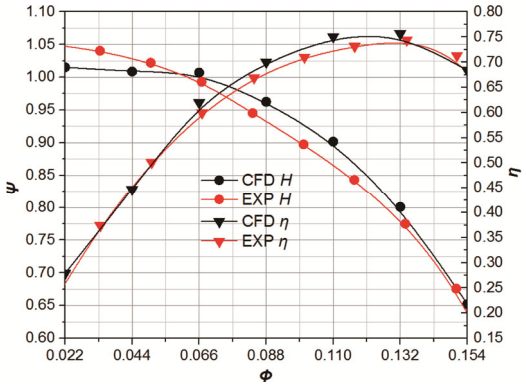

Fig. 17 Numerical and test results of performance curves

7.2 Test of self-priming

For investigating the self-priming performance of the novel self-priming pump, the tests of the different self-priming heights are performed respectively. Table 4 lists the average self-priming time after repeated tests. It can be found that the self-priming time is obviously shorter than the traditional self-priming pump, and the performance of self-priming is remarkably superior to the national standard. Thus, the self-priming ability is significantly improved by employing the novel jet self-priming system.

Fig. 18 Self-priming test under different height

Table 4 Result of the self-priming test

Height	6 m	7 m	8 m
Self-priming time	92 s	121 s	173 s

8. Conclusions

In this paper, the self-priming performance is significantly improved by employing the novel jet self-priming system. The optimal thickness distribution of the blade is obtained by systematical and theoretical analysis. The conclusions are obtained as follow:

1. The novel self-priming pump is proposed. The quick self-priming velocity and the self-closing of jet self-priming can be achieved by the well coordination between the jet nozzle and globe value. The self-priming test is performed under 6 m, 7 m and 8 m, and the performance of self-priming is remarkably superior to the national standard.

2. The internal field characteristic of blades with different thickness distribution are analyzed, and the obvious elliptical high-pressure area (EHPA) are found at the trialing edge of the thicker blade under small flow rates. It ascribes to that the positive angle of attack is generated, and the control of the fluid boundary layer on the blade surface is insufficient, which results in the separation of the unstable boundary layer at the blade outlet. The EHPA of each scheme on the working surface are vanished at the design flow rate. When the flow rate increases to 700 m^3/h, gradient of pressure distribution on the working surface becomes more uniform, and the local low-pressure can be founded on the trailing edge of blade with increment thickness distribution of working surface. The relative velocity at the trialing edge is high under large flow rates, and the liquid in the volute flows according to free vortex theory. The velocity vector at the blade trailing edge changes significantly.

3. The energy loss is investigated based on the entropy production theory. It is concluded that the flow rate has the different influence on the three types of entropy production, and the turbulent entropy production and viscosity entropy production are greater than the wall entropy production, which can be regarded as the major factors leading to the hydraulic loss. The blade employs the decrement distribution thickness from leading edge to the trailing edge, which can not only give rise to obvious separation of the boundary layer under small flow rates, but also generates the strong impact at the leading edge under the large flow conditions. The similar conclusions are verified by the analysis of hydraulic performance, and the test is performed to benchmark the credibility of the simulation.

4. Compared with the pressure pulsation on the working surface of the blade, it is found that with the flow rates increasing, the amplitude of pressure pulsation firstly decreases and then smoothly improves, and reaches the minimum under design flow rate. By systematically analyzing the energy loss and the pressure pulsation among the different schemes, the optimal blades are obtained. The blade with thickness distribution of 3-6-6 can satisfy the requirements of the ideal liquid flow, and the liquid could flow according to the designed speed direction. Moreover, the optimal thickness distribution of the blades can effectively improve the pressure pulsation characteristics, and ensure the blades operating under the safe and stable condition.

Acknowledgments

The authors gratefully acknowledge the support from the National Natural Science Foundation of China (No.51679111, No.51409127 and No.51579118), Six Talents Peak Project of Jiangsu Province JNHB-CXTD-005, Natural Science Foundation of Jiangsu Province (BE2016163, BRA2017353 and No.BK20161472), Scientific research project of Jiangsu University

(No.17A302), Priority Academic Program Development of Jiangsu Higher Education Institutions (PAPD) and National Key R&D Program Project (No.2017YFC0403703).

References

[1] Kifle M., Gebremicael T.G., Girmay A., et al., Effect of surge flow and alternate irrigation on the irrigation efficiency and water productivity of onion in the semi-arid areas of North Ethiopia. Agricultural Water Management, 2017, 187: 69–76.

[2] Chen H,, Gao Z,, Zeng W,, et al., Scale Effects of water saving on irrigation efficiency: case study of a rice-based groundwater irrigation system on the Sanjiang plain, Northeast China. Sustainability, 2017, 10(1): 47.

[3] Wang C., Shi W., Wang X., et al., Optimal design of multistage centrifugal pump based on the combined energy loss model and computational fluid dynamics. Applied Energy, 2017, 187: 10–26.

[4] Lim S.E., Chang H.S., CFD analysis of performance change in accordance with inner surface roughness of a double-entry centrifugal pump. Journal of Mechanical Science & Technology, 2018, 32 (2): 697–702.

[5] Zhang J.Y., Cai S.J., Li Y.J., et al., Optimization design of multiphase pump impeller based on combined genetic algorithm and boundary vortex flux diagnosis. Journal of Hydrodynamics, 2017, 29 (6):1023–1034.

[6] Wang T., Kong F., Xia B., et al., The method for determining blade inlet angle of special impeller using in turbine mode of centrifugal pump as turbine. Renewable Energy, 2017, 109: 518–528.

[7] Jeon S.Y., Kim C.K., Lee S.M., et al., Performance enhancement of a pump impeller using optimal design method. Journal of Thermal Science, 2017, 26 (2): 119–124.

[8] Li W., Zhao X., Li W., et al., Numerical prediction and Performance experiment in an engine cooling water pump with different blade outlet widths. Mathematical Problems in Engineering, 2017, 2017(6): 1–11.

[9] Bejan A., Kestin J., Bejan A., Entropy generation through heat and fluid flow. Journal of Applied Mechanics, 1983, 50 (2): 475.

[10] Li D., Wang H., Qin Y., et al., Entropy production analysis of hysteresis characteristic of a pump-turbine model. Energy Conversion & Management, 2017, 149: 175–191.

[11] Hou H., Zhang Y., Li Z., et al., Numerical analysis of entropy production on a LNG cryogenic submerged pump. Journal of Natural Gas Science & Engineering, 2016, 36: 87–96.

[12] Herwig H., Gloss D., Wenterodt T., A new approach to understanding and modelling the influence of wall roughness on friction factors for pipe and channel flows. Journal of Fluid Mechanics, 2008, 613(613): 35–53.

[13] Kock F., Herwig H., Local entropy production in turbulent shear flows: a high-Reynolds number model with wall functions. International Journal of Heat & Mass Transfer, 2004, 47(10): 2205–2215.

[14] Pei J., Meng F., Li Y., et al., Effects of distance between impeller and guide vane on losses in a low head pump by entropy production analysis. Advances in Mechanical Engineering, 2016, 8(11): 1–11.

[15] Wang C., Effect and experiment of different blade thickness on stainless steel stamping well pump performance. Transactions of the Chinese society for agricultural machinery, 2012, 43(7): 94–99.

[16] Pinto R.N., Afzal A., D'Souza L.V., et al., Computational fluid dynamics in turbomachinery: a review of state of the art. Archives of Computational Methods in Engineering, 2017, 24(3): 467–479.

[17] Spurk D.I.J.H., Str mungslehre. Berlin: Springer, 1989.

[18] Gong R.Z., Wang H.J., Chen L.X., et al., Application of entropy production theory to hydro-turbine hydraulic analysis. Science China, 2013, 56(7): 1636–1643.

[19] Zhang X., Wang Y., Xu X., et al., Energy conversion characteristic within impeller of low specific speed centrifugal pump. Transactions of the Chinese Society for Agricultural Machinery, 2011, 42(7): 75–81.

[20] Tao Y., Yuan S., Liu J., et al., Influence of blade thickness on transient flow characteristics of centrifugal slurry pump with semi-open impeller. Chinese Journal of Mechanical Engineering, 2016, 29(6): 1–9.

[21] Zheng L., Dou H.S., Chen X., et al., Pressure fluctuation generated by the interaction of blade and tongue. Journal of Thermal Science, 2018, 27(1): 8–16.

[22] Jia X.Q., Cui B.L., Zhu Z.C., et al., Numerical investigation of pressure distribution in a low specific speed centrifugal pump. Thermal Science, 2018, 27(1): 25–33.

[23] Zhai J., Zhu B., Li K., et al., Internal pressure fluctuation characteristic of low specific speed mixed flow pump. Transactions of the Chinese Society for Agricultural Machinery, 2016, 47(6): 42-46.